MODELLING TURBULENT COMBUSTION COUPLED WITH CONJUGATE HEAT TRANSFER IN OPENFOAM

M. el Abbassi[a,*], D.J.P. Lahaye[*], C. Vuik[*]
[a]m.elabbassi@tudelft.nl
*Delft University of Technology, Delft Institute of Applied Mathematics, Delft, The Netherlands

Abstract
This paper verifies a mathematical model that is developed for the open source CFD-toolbox OpenFOAM, which couples turbulent combustion with conjugate heat transfer. This feature already exists in well-known commercial codes. It permits the prediction of the flame's characteristics, its emissions, and the consequent heat transfer between fluids and solids via radiation, convection, and conduction. The verification is based on simplified 2D axisymmetric cylindrical reactors. In the first step, the combustion part of the solver is compared against experimental data for an open turbulent flame. This shows good agreement when using the full GRI 3.0 mechanism. Afterwards, the flame is confined by a cylindrical wall and simultaneously conjugate heat transfer is activated and analysed. Finally, a backward facing step is included to increase flow complexity and the results are compared with the commercial CFD code ANSYS Fluent. It is shown that the combustion and conjugate heat transfer are successfully coupled. When radiation is disabled, comparable results are achieved by both solvers, while enabling radiation leads to larger discrepancies.

Introduction
Industrial furnaces such as kilns are pyroprocessing devices in which a heat source is generated via fuel combustion. In order to make a numerical prediction of the temperature distribution along a solid (e.g. the material bed, furnace walls, or heat exchanger), one must model the coupled effects of the occurring physical phenomena. The heat released by the fluctuating turbulent flame may be transferred to the solid through all heat transfer modes: thermal radiation, conduction, and convection. Thermal radiation is transmitted to the solid directly from the flame, or indirectly from the hot exhaust and other solids. Conduction occurs within solids and through contact with other solid particles, while convective heat may be exchanged via any contact between gas and solids. In return, the fluctuating heat transfer affects the turbulent flow and flame characteristics. Controlling the flame enables achieving the desired heat distribution with minimum emissions. Coupling combustion and heat transfer is essential to find optimal solutions to these conflicting interests, particularly in view of increasing environmental concerns (which view reducing the furnace emissions and fuel consumption as urgent), along with the growing demand for an increase in furnace production rate.

Incorporating the heat transfer between fluids and solids into one mathematical problem may be referred as conjugate heat transfer (CHT). CHT is implemented in many popular CFD codes. There are several publications available on furnace models where combustion and CHT are coupled. For example, in the work of Pisaroni, Lahaye and Sadi [1], the prediction of the furnace wall heat distribution was made with CD-Adapco's STAR-CCM+. Gao et al [2] used ANSYS-CFX to model the heat distribution, while ANSYS-Fluent was the CFD-tool for the works of other researchers [3, 4, 5].

To date, there are no publications on coupling turbulent combustion and CHT with the open source CFD-toolbox OpenFOAM. OpenFOAM sets a structured object-oriented framework and includes numerous applications to solve different kinds of CFD-related problems. The source code is fully accessible and allows building new or modified applications while making use of

existing libraries, models and utilities to link them. OpenFOAM also allows high performance computing using e.g. MPI and GPU's that do not include any license costs, and hence may lead to significant savings for large and complex problems. There are numerous studies in which combustion solvers of OpenFOAM were benchmarked against different experiments and other solvers (e.g. [6, 7, 8, 9]) and some include thermal radiation for the heat transfer (e.g. [10]). The capabilities of OpenFOAM's CHT solver have also been studied extensively and some recent investigations into this matter, (with and without radiative heat transfer) can be found in [11, 12, 13, 14].

Although all the necessary libraries are available in OpenFOAM to model the required physical phenomena, there is currently no standard implementation available in the existing releases that couples combustion and CHT. However, an implementation was recently proposed and developed for OpenFOAM by Tonkomo LLC [15, 16], that combines the turbulent-non-premixed-combustion solver reactingFoam with the CHT-solver chtMultiRegionFoam. This provides new opportunities for modelling furnaces or any other combustion and heat transfer related problem. In our work, the capabilities of the new solver are investigated by testing it on different 2D axisymmetric cases, in increasing order of complexity, by means of RANS simulation. The first case is an open turbulent flame from the Sandia laboratory which is used to validate the solver's implementation of turbulent combustion. Afterwards, CHT is also activated by adding a cylindrical solid region that represents the furnace wall. This way, the effect of the walls on the flame characteristics can be analysed and the heat distribution on the wall can be determined. The results are then compared with the ones generated by ANSYS-Fluent.

Our presented work is structured as follows. First the governing equations of the problem are highlighted, and we describe the physical models of OpenFOAM that are needed to solve them. Second, the coupling of combustion and conjugate heat transfer is explained. Third, the cases and their boundary conditions are presented, followed by a discussion of the results.

Governing equations and numerical models

In the fluid domain, the Favre-averaged transport equations of mass, momentum, sensible enthalpy and chemical species [17] are respectively described by

$$\frac{\partial(\bar{\rho})}{\partial t} + \nabla \cdot (\bar{\rho}\widetilde{u}) = 0, \tag{1}$$

$$\frac{\partial(\bar{\rho}\widetilde{u})}{\partial t} + \nabla \cdot (\bar{\rho}\widetilde{u}\widetilde{u}) = [-\nabla\bar{p} + \nabla \cdot \bar{\tau}] - \nabla \cdot \bar{\rho}\widetilde{u"u"}, \tag{2}$$

$$\frac{\partial(\bar{\rho}\widetilde{h})}{\partial t} + \nabla \cdot (\bar{\rho}\widetilde{u}\widetilde{h}) = \frac{D}{Dt}p + \nabla \cdot (\frac{\lambda}{c_p}\nabla\widetilde{h} - \bar{\rho}\widetilde{h"u"}) + \widetilde{Q}, \tag{3}$$

$$\frac{\partial(\bar{\rho}\widetilde{Y_\alpha})}{\partial t} + \nabla \cdot (\bar{\rho}\widetilde{u}\widetilde{Y}_\alpha) = \nabla \cdot \rho\Gamma\nabla Y_\alpha + \widetilde{R}_\alpha - \nabla \cdot \bar{\rho}\widetilde{Y_\alpha"u"}, \tag{4}$$

where ρ is the density, u the velocity, p the pressure, τ the shear stress tensor, h the specific sensible enthalpy, λ the fluid conductivity, c_p the specific heat capacity at constant pressure, Q a heat source, Y_α the species mass fraction of species α, Γ the species diffusion coefficient and R the reaction rate of species α. The over-bar and tilde notations stand for the average values, while the double quotation marks denote the fluctuating components due to turbulence. Note that several source terms (such as body forces and viscous heating) are neglected.

For solid regions, only the energy transfer needs to be solved and therefore the equation of enthalpy for solids, which is the following heat equation, has to be added to the list of transport

equations 1-4:

$$\frac{\partial(\bar{\rho}h)}{\partial t} = \nabla \cdot (\lambda_s \nabla T) + Q, \tag{5}$$

where λ_s is the solid thermal conductivity and T the temperature. Except for equation 5, unclosed terms appear due to the Favre averaging that will be treated here.

Turbulence

The unknown Reynolds stresses (last term of equation 2) are solved by employing the Boussinesq hypothesis that is based on the assumption that in turbulent flows, the relation between the Reynolds stress and viscosity is similar to that of the stress tensor in laminar flows, but with increased (turbulent) viscosity:

$$-\nabla \cdot \bar{\rho}\widetilde{u_i" u_j"} = \mu_t \left(\frac{\partial u_i}{\partial x_j} + \frac{\partial u_j}{\partial x_i} \right) - \frac{2}{3} \left(\rho k + \mu_t \frac{\partial u_k}{\partial x_k} \right) \delta_{ij}, \tag{6}$$

where μ_t is the turbulent viscosity and k the turbulent kinetic energy. The Reynolds stresses are closed with the Realizable k-ϵ turbulence model [18], which is widely known for its superior capability over the Standard and RNG k-ϵ models in predicting the mean of the more complex flow features. The model solves two additional transport equations: one for the turbulent kinetic energy k, and the other for its dissipation rate ϵ

$$\frac{\partial(\bar{\rho}k)}{\partial t} + \nabla \cdot (\bar{\rho}\widetilde{u}k) = \nabla \cdot \left[\left(\mu + \frac{\mu_t}{\theta_k} \right) \nabla k \right] + \mu_t \left(\frac{\partial u_i}{\partial x_j} \right)^2 - \bar{\rho}\epsilon, \tag{7}$$

$$\frac{\partial(\bar{\rho}\epsilon)}{\partial t} + \nabla \cdot (\bar{\rho}\widetilde{u}\epsilon) = \nabla \cdot \left[\left(\mu + \frac{\mu_t}{\theta_\epsilon} \right) \nabla \epsilon \right] + \bar{\rho}c_1 S\epsilon - \bar{\rho}c_2 \frac{\epsilon^2}{k + \sqrt{\nu\epsilon}}, \tag{8}$$

where θ_k,θ_ϵ and c_2 are constants. S is the modulus of the mean strain rate tensor, defined as $S = \sqrt{2S_{ij}S_{ij}}$ and c_1 is a function of k, ϵ and S. Again, note that the effect of buoyancy and other source terms are neglected. With k and ϵ, the turbulent viscosity can be determined by the following relation:

$$\mu_t = \bar{\rho}c_\mu \frac{k^2}{\epsilon}, \tag{9}$$

where in the Realizable k-ϵ model, c_μ is a function of k, ϵ, the mean strain rate and the mean rotation rate. This is one of the major differences compared to the other k-ϵ models where c_μ is a constant.

The turbulent scalar fluxes $\bar{\rho}\widetilde{\phi" u"}$ for the scalar chemical species and scalar sensible enthalpy (both denoted as ϕ) are closed with the Gradient diffusion assumption

$$-\bar{\rho}\widetilde{\phi" u"} = \nabla \cdot (\Gamma_t \widetilde{\phi}), \tag{10}$$

where Γ_t is the turbulent diffusivity determined by (assuming Lewis number = 1) the turbulent viscosity μ_t and turbulent Prandtl number Pr_t: $\Gamma_t = \mu_t / Pr_t$.

Combustion

The mean chemical source term $\widetilde{R}_\alpha$ is closed with the Partially Stirred Reactor (PaSR) model. The model developed at Chalmers university (see [19] for the full derivation) allows for the detailed Arrhenius chemical kinetics to be incorporated in turbulent reacting flows. It assumes that each cell is divided into a non-reacting part and a reaction zone that is treated as a perfectly stirred reactor. The fraction is proportional to the ratio of the chemical reaction time t_c to the

total conversion time $t_c + t_{mix}$:

$$\gamma = \frac{t_c}{t_c + t_{mix}}. \tag{11}$$

The turbulence mixing time t_{mix} characterizes the exchange process between the reacting and non-reacting mixture, and is determined via the k-ϵ model as

$$t_{mix} = c_{mix}\sqrt{\frac{\mu_{eff}}{\bar{\rho}\epsilon}}, \tag{12}$$

where c_{mix} is a constant and μ_{eff} is the sum of the laminar and turbulent viscosity. Then the mean source term is calculated as $\widetilde{R}_\alpha = \gamma R_\alpha$, where R_α is the laminar reaction rate of species α and is computed as the sum of the Arrhenius reaction rates over the N_R reactions that the species participate in:

$$R_\alpha = \sum_{r=1}^{N_R} \hat{R}_{\alpha,r}, \tag{13}$$

where $\hat{R}_{\alpha,r}$ is the Arrhenius rate of creation/destruction of species α in reaction *r*. For a reversible reaction, the Arrhenius rate is given by

$$\hat{R}_{\alpha,r} = \psi_{f,r}\prod_{r=1}^{N_R}[C_{\beta,r}]^{\eta'_{\ell,r}} - \psi_{b,r}\prod_{r=1}^{N_R}[C_{\beta,r}]^{\eta''_{m,r}}, \tag{14}$$

where $C_{\beta,r}$ is the concentration of species β in reaction *r*, $\eta'_{\ell,r}$ is the rate exponent for reactant ℓ in reaction *r*, $\eta''_{m,r}$ is the stoichiometric coefficient for product m in reaction *r*, and $\psi_{f,r}$ and $\psi_{b,r}$ are respectively the forward and backward rate constants given by the Arrhenius expressions.

The chemical time scale can be determined with the following relation:

$$\frac{1}{t_c} = max\left(\frac{-\partial R_\alpha}{\partial Y_\alpha}\frac{1}{\bar{\rho}}\right). \tag{15}$$

Energy

The thermal conductivity λ in the averaged transport of sensible enthalpy (equation 3) is replaced by the effective conductivity λ_{eff}, which incorporates the unknown turbulent scalar flux. Using equation 10, λ_{eff} is defined by the Standard and Realizable k-ϵ models as

$$\lambda_{eff} = \frac{\mu}{Pr} + \frac{\mu_t}{Pr_t}, \tag{16}$$

where the turbulent Prandtl number, from experimental data, has and average value of 0.85. The mean source term $\widetilde{Q}$ can be split up into the heat sources due to combustion and radiation. The combustion heat source follows from the calculation of the mean species source term (enthalpy of formation). The mean radiative source term is elaborated in the following section.

Radiation

Mathematically, the Radiative Transfer Equation (RTE) for an emitting-absorbing-scattering non-grey medium is described as

$$\frac{dI_\chi(\vec{r},\vec{s})}{ds} = \underbrace{-\kappa_\chi I_\chi(\vec{r},\vec{s})}_{\text{absorption}} + \underbrace{\kappa_\chi I_{b\chi}(\vec{r})}_{\text{emission}} - \underbrace{\xi_\chi I_\chi(\vec{r},\vec{s})}_{\text{'out' scattering}} + \underbrace{\frac{\xi_\chi}{4\pi}\int_{4\pi} I_\chi(\vec{r},\vec{s}^*)\Phi(\vec{s}^*,\vec{s})d\Omega^*}_{\text{'in' scattering}}, \tag{17}$$

where for each wavelength χ, I is the spectral radiation intensity at point $\vec{r}$ propagating along direction $\vec{s}$, κ and ξ are respectively the absorption and scattering coefficients of the medium, and $\Phi(\vec{s}^*, \vec{s})$ is the scattering phase function. The ratio $\Phi(\vec{s}^*, \vec{s})/4\pi$ represents the probability that radiation propagates in direction $\vec{s}^*$ and is confined within solid angle $d\Omega^*$. The black-body intensity I_b is given by Planck's law:

$$I_{b\chi} = \frac{c_1}{\pi\chi^5(exp(c_2/(\chi T) - 1)}, \tag{18}$$

where c_1 and c_2 are constants. In combustion systems where the fuel is a gas, scattering can be neglected, hence the last two terms of equation 17 are left out.

To obtain the divergence of the radiative heat flux $\nabla \cdot q_R$ as the source term for the enthalpy transport equation, the RTE is integrated in both spectral variable and solid angle of 4π. The Discrete Ordinates Method (DOM) solves the RTE for a set of discrete directions, which span the total solid angle range of 4π around a point in space. The integrals over solid angles are approximated using a numerical quadrature rule. Therefore, the RTE may be written as follows for direction $\vec{s}^m$:

$$\frac{dI^m}{ds} = -\kappa_\chi I^m + \kappa_\chi I_b, \tag{19}$$

where superscript m ($1 \leq m \leq M$) denotes the m-th direction and M is the total number of discrete directions.

To solve equation 19, the local absorption coefficient of the gas mixture has to be determined. This is a function of gas composition, temperature, wavelength, and pressure. Within the radiation spectrum, the individual species absorb and emit through thousands of wavelengths, which makes it too expensive to calculate for all of them. Although models exist that average the amount of the wavelength lines up to a handful of broad bands (Wide Band Model), we chose to apply the grey gas assumption where the absorption coefficient is an average over the whole spectrum. This is a crude simplification and may lead to significant errors [20]. Nevertheless, the model still accounts for the gas composition, temperature and pressure so that the absorption coefficient can be calculated with a polynomial for each species,

$$\kappa_\alpha = \sum_{p=1}^{6} a_{p,\alpha} \cdot T^{p-1}, \tag{20}$$

where T is the local gas temperature and the polynomial coefficients $a_{p,\alpha}$ are specified for species α at a certain pressure.

Radiation has to be treated differently when considering solids. In combustion systems solid boundaries are generally opaque and may be assumed to be grey and diffuse [20]. A property of grey bodies is that they are independent of the spectral variable (e.g. wavelength). If the solid is diffuse, its radiative properties are also independent of direction, so that emission and reflection happen diffusely (neglecting specular reflection). The boundary condition will be [21]

$$I_{s\chi}(\vec{s}) = \kappa_s I_{bs} + \frac{1 - \kappa_s}{\pi} \int_{\vec{n}\cdot\vec{s}<0} I_s(\vec{s})|\vec{n} \cdot \vec{s}|d\Omega, \tag{21}$$

where the subscript s denotes the solid-region and κ_s is the solid emissivity.

Summary

In short, the following physical models for the solver are chosen for the test cases. The Reynolds stresses are closed with the Realizable k-ϵ model, and the PaSR model was used for the mean

species source term. The 2-step Westbrook and Dryer reaction mechanism [22] is used for all test cases, while the GRI 3.0 mechanism [23] is only used for validation. The mean radiative heat source is modelled using the DOM and the species emissivities are determined with OpenFOAM's sub-model greyMeanAbsorptionEmission.

Conjugate heat transfer

Now that equations have been treated individually for the fluid and solid domains, the thermal energy transport must be coupled. This is also known as conjugate heat transfer (CHT). The classic method for calculating the heat transfer between a fluid and a solid is based on the proportional relation of the heat flux to the heat transfer coefficient and the temperature difference between wall and gas. The convective heat transfer coefficient is related to the Nusselt number, which is derived from empirical relations. To replace the empirical relations, methods have been developed that are based on a strictly mathematically-stated problem, describing the heat transfer between solid and fluid domains as a result of their interaction. To solve CHT problems, two important conditions are required at the interface of the domains to ensure continuity of both the temperature and heat flux:

$$T_{f,int} = T_{s,int} \tag{22}$$

and

$$\lambda_f \frac{\partial T_f}{\partial y}\bigg|_{int,y=+0} = \lambda_s \frac{\partial T_s}{\partial y}\bigg|_{int,y=-0}, \tag{23}$$

where the subscripts f, s and int respectively stand for fluid, solid and interface. y is the local coordinate normal to the solid. The three heat transfer modes needed to calculate the heat transfer at the interface will be elaborated in the following subsections.

Convective heat transfer

An idea to calculate the convective heat transfer in turbulent flows would be to replace λ_f in equation 23 with the effective conductivity λ_{eff}, and to solve the temperature at the wall adjacent cell. However, k-ϵ models do not account for wall dampening effects due to the no-slip condition. Normally in free stream flow, viscous stresses are negligible compared to Reynolds stresses. However, close to the wall, the wall shear stress dampens out the velocity fluctuations, and at the wall, where $\vec{u}_i = 0$, the Reynolds stresses are also zero. This means that the total shear stress at the wall is due to the viscous contribution, which also causes the mean velocity profile at the boundary layer to be logarithmic. Even other two-equation turbulence models that do incorporate wall dampening are unable to predict this accurately, unless the wall is extremely refined to capture the very sharp velocity gradients and the complex three-dimensional flow near the wall. This would require a substantial increase in computational power to solve. An alternative is to apply wall functions that make use of the universal behaviour of the flow near the wall [21]. Assuming that the flow behaves like a fully developed boundary layer, the gradients of both the velocity and temperature at the cells adjacent to the wall interface boundary can be well predicted without a need for extreme refinement near the wall.

Wall functions

The foundation of the standard wall functions comes from the 'Law of the wall' (or the log law), which states that the average velocity of the turbulent flow near the wall is proportional to the logarithm of the normal distance from the wall. The log law was first published by von Kármán and is governed by the following relation

$$u^+ = \frac{1}{K} \ln(Ey^+), \tag{24}$$

where the constant K is known as the Von Kármán constant and, based on experiments, is equal to $K \approx 0.41$. The wall roughness parameter E is equal to $E \approx 9.8$ for smooth walls, and for rough walls other values can be assigned. y^+ is the non-dimensional normal distance from the wall and u^+ is the non-dimensional velocity parallel to the wall, determined by

$$y^+ = \frac{yu_\tau}{\nu} \qquad u^+ = \frac{u}{u_\tau} \qquad u_\tau = \sqrt{\frac{\tau_w}{\bar{\rho}}}, \tag{25}$$

where u_τ is the friction velocity and τ_w is the wall shear stress. By making use of the log law, it can be derived that (see e.g. [24], [25]) the kinetic energy and energy dissipation at the wall adjacent cells can be found with the following relations

$$k_P = \frac{u_\tau^2}{\sqrt{c_\mu}} \qquad \epsilon_P = \frac{u_\tau^3}{Ky}, \tag{26}$$

where the subscript P denotes the cell node coordinate adjacent to the wall. Using equations 9 and 16, μ_t and λ_{eff} in the boundary layer can also be found.

Thermal conduction
Heat transfer to the wall boundary from a solid cell is computed as

$$q = \frac{\lambda_s}{\Delta n}(T_w - T_s), \tag{27}$$

where λ_s and T_s are the thermal conductivity and local temperature of the solid respectively, and Δn is the distance between wall surface and the solid cell centre.

Radiative heat transfer
Adding radiation to the problem and integrating equation 21 alters the interface condition 23 to:

- from fluid to solid

$$\lambda_{eff}\frac{\partial T_f}{\partial y}\bigg|_{int,y=+0} + q_{rad,in} = \lambda_s\frac{\partial T_s}{\partial y}\bigg|_{int,y=-0}, \tag{28}$$

- from solid to fluid

$$\lambda_{eff}\frac{\partial T_f}{\partial y}\bigg|_{int,y=+0} = \lambda_s\frac{\partial T_s}{\partial y}\bigg|_{int,y=-0} - q_{rad,out}, \tag{29}$$

where $q_{rad,in}$ is the incident radiative heat flux

$$q_{rad,in} = \int_{\vec{n}\cdot\vec{s}<0} I_s(\vec{s})|\vec{n}\cdot\vec{s}|d\Omega \tag{30}$$

and $q_{rad,out}$ is the radiative heat flux leaving the solid surface

$$q_{rad,out} = \frac{1}{\pi}\left[\kappa_s\sigma T^4 + (1-\kappa_s)q_{rad,in}\right], \tag{31}$$

where σ is the Stefan–Boltzmann constant 5.670373×10^{-8} $\mathrm{Wm^{-2}K^{-4}}$

Conjugation
Dorfman [26] describes different methods to perform conjugation between the solution domains of which OpenFOAM's current standard solver chtMultiRegionFoam applies the iterative

method, where the equations of the fluid and solid domains are solved separately. The idea of this approach is that each solution for one of the domains produces a boundary condition along the interface for the other. The process starts by solving the fluid domains in assigned order, with an initial guess of the temperature distribution at the interface. The heat flux distribution obtained at the interfaces is then used to solve the energy transport in the solid domains and to obtain a new temperature distribution, and so on. If this process converges, the iterations continue until a desired accuracy is achieved. However, depending on the domain sizes, the rate of convergence may depend highly on the initial guess.

Numerical Set-up

Test cases

The solver is tested on three methane-air combustion cases. In the first case, the implementation of combustion in the new solver is validated with experimental data from a turbulent piloted diffusion flame from the Sandia National Laboratories (Sandia Flame D). The burner dimensions can be found here [27].

For the second case, CHT is activated and the Sandia Flame D is confined by a cylindrical wall made of refractory material, with inner and outer diameters of respectively 300 and 360 mm. The axial length of the calculation domain (excluding fuel and pilot channels) is 600 mm. The boundary conditions of the two cases can be found in Table 1, and the wall dimensions and properties are shown in Table 2.

As a the third case, a geometry is designed to introduce circulation in the flow. For this reactor, the dimensions are adopted from the Burner Flow Reactor (BFR) in [28], with some major differences. Rather than using swirling air for flame stabilization, we chose to use hot co-flow that is injected axially. We left out the narrowed exhaust pipe to increase the adverse pressure gradient along the central axis, causing the jet to decelerate more, and thus further improve flame stability. The notion behind these modifications is to have a simpler flow, similar to that of a backward facing step, which we can better understand in 2D. The final geometry is shown schematically in Fig. 1, where the fuel channel diameter is $10\,$mm and the hot co-flow inner and outer diameters are respectively $11\,$mm and $200\,$mm. The fuel tube has a wall thickness of $0.5\,$mm. The boundary conditions are shown in Table 3 and the wall material is the same as for case 2. The operating power is 200 kW with a fuel-air equivalence ratio of 0.8.

Table 1: Boundary and initial conditions for Sandia Flame D. zG stands for the Neumann boundary condition zeroGradient. The axial-velocities are expressed in m/s, and the temperatures in K. Species are denoted in mass fractions.

Variable	Fuel jet	Pilot jet	Co-flow	Gas-wall interface	Outer wall surface	Side wall surfaces
U_{axial} (m/s)	49.6	11.4	0.9	0	-	-
T (K)	294	1880	291	Coupled	291	zG
Y_{CH_4}	0.1561	0	0	zG	-	-
Y_{O_2}	0.1966	0.054	0.23	zG	-	-
Y_{N_2}	0.6473	0.742	0.77	zG	-	-
Y_{H_2O}	0	0.0942	0	zG	-	-
Y_{CO_2}	0	0.1098	0	zG	-	-

Numerical methods

The computational domains of cases 1 to 3 consist of respectively 38000, 45000 and 43000 quadrilateral cells. The 1st order implicit Euler discretization scheme is used for the unsteady terms and a central differencing scheme for the gradient and Laplacian terms. The convection

Table 2: Thermal properties of the refractory material.

Density ρ	Thermal conductivity λ_s	specific heat capacity c_p	emissivity κ_s
$2800\,\mathrm{kgm^{-3}}$	$2.1\,\mathrm{Wm^{-1}K^{-1}}$	$860\,\mathrm{Jkg^{-1}K^{-1}}$	$0.6\,\mathrm{m^{-1}}$

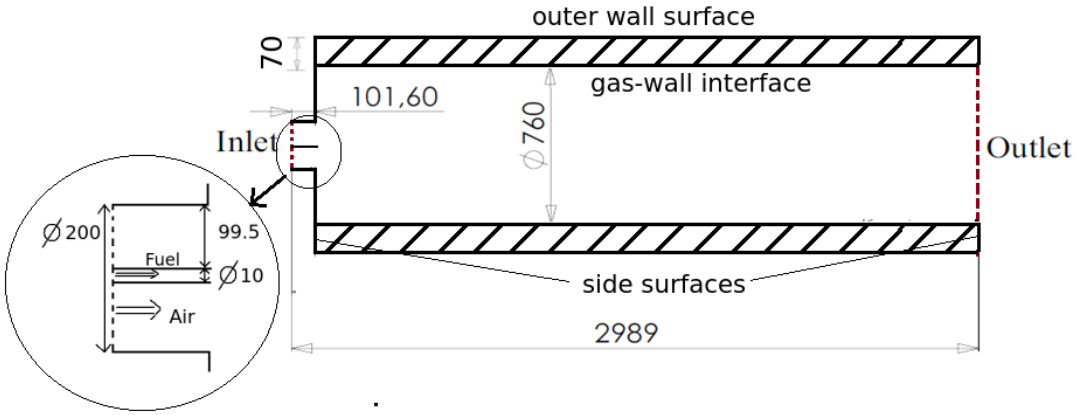

Figure 1: Schematic geometry of the modified BFR. Dimensions are denoted in mm.

Table 3: Boundary and initial conditions for the modified BFR. zG stands for the Neumann boundary condition zeroGradient. The axial-velocities are expressed in m/s, and the temperatures in K. Species are denoted in mass fractions.

Variable	fuel jet	co-flow	gas-wall interface	outer wall surface	side wall surfaces
U_{axial} (m/s)	82.22	6.619	0	-	-
T (K)	300	800	Coupled	300	zG
Y_{CH_4}	1	0	zG	-	-
Y_{O_2}	0	0.234	zG	-	-
Y_{N_2}	0	0.766	zG	-	-

terms for velocity, enthalpy, chemical species and radiation intensity are discretized using the 2nd order upwind scheme while for the kinetic energy and energy dissipation this is done with the 1st order upwind scheme. The time step is determined from the max Courant number which is set to 0.4.

The generated linear system of equations is solved as follows. The mass fluxes are solved using the Preconditioned Conjugate Gradient (PCG) method using the diagonal incomplete Cholesky factorization as preconditioner, while the equations for pressure and radiation intensity are solved with the geometric-algebraic multi-grid method. The remaining variables are solved with the Preconditioned Bi-CG (PBiCG) method and using the diagonal incomplete LU factorization as preconditioner, which is suitable for non-symmetric sparse matrices caused by the convection terms.

Simulation procedure

The simulations run until convergence is observed with the maximum gas temperature, maximum solid temperature, average outlet temperature and average outlet CO_2 fraction. The computation starts with a solved non-reacting turbulent flow field as initial state. It is observed that for cases 1 and 2 the solution converges after 0.15 s in physical time, whereas for case 3 this is after 0.3 s.

Verification with ANSYS-Fluent®

In order to verify the new solver, the results of case 3 are compared with the results of ANSYS-Fluent. The test-case in Fluent is therefore set-up as close as possible to that of multiRegion-ReactingFoam. However, there are two major differences: the combustion model PaSR and the radiation sub-model greyMeanAbsorptionEmission are not available in Fluent. Therefore, the combustion model of choice for Fluent is the Eddy Dissipation Concept model, which for the most part shares its philosophy with the PaSR model. The gas mixture's absorption coefficients are computed with a more advanced grey gas assumption model, the Weighted Sum of Gray Gases (WSGG), where the absorption coefficients also depend on beam length and partial pressures of the gas species.

Results and discussion

Case 1

In Fig. 2 the temperature along the axis of symmetry is plotted. It shows that the multiRegionReactingFoam's prediction is identical to that of reactingFoam, as would be expected when CHT is switched of. Both solvers over-predict the ignition delay, temperature rise and peak temperature with the 2-step reaction mechanism. When using the full GRI mechanism, these features are better captured and show good agreement.

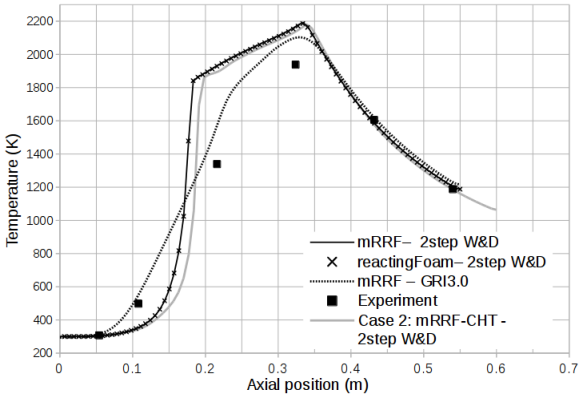

Figure 2: Temperature progression along the centre line (Case 1).

Figure 3: Contour plot of the temperature (Case 2).

Case 2

Now that a wall is introduced around the Sandia Flame D, it absorbs some of the energy, as can be seen in Fig. 3. Fig. 4 shows a decomposition of the heat transfer to the wall in which the wall is being heated only due to thermal radiation. The wall is not heated via convection due to the fact that the hot gas heated by the flame leaves the domain before coming into contact with the wall. In fact, the convective heat transfer part plays a cooling role by transferring some of the wall's heat to the cold adjacent air, hence the negative contribution. The radiative energy absorption by the wall has an additional cooling effect on the flame, as can be seen in Fig. 2.

Case 3

For this case, first a comparison is made with a non-reacting flow. Fig. 5 shows the agreement of the cold flow velocity profiles predicted by both solvers. A small difference can be noticed in maximum velocity at the centre line. For the second comparison, combustion is included without thermal radiation. In the contour plot of the temperature (Fig. 7), similar flame characteristics can be noticed, such as the flame's length and position. Although the maximum temperature differs only by 23 K, the hot spots are located at different regions. This is influenced by the different prediction of the temperature distribution (and probably also by the species and

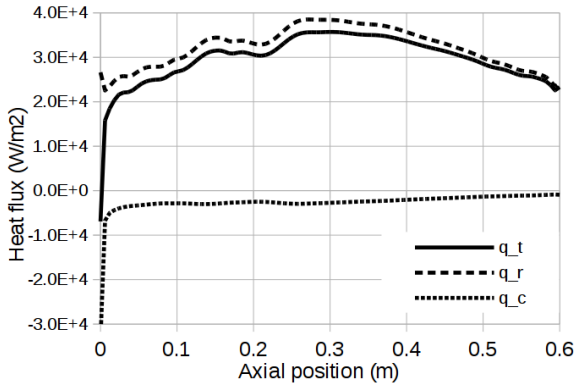

Figure 4: Heat flux along the inner wall surface (Case 2). q_t, q_r and q_c are respectively the total, radiative and convective heat fluxes.

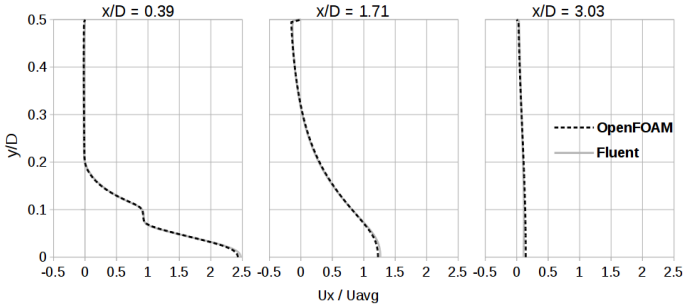

Figure 5: Comparison of the axial velocity profiles plotted in radial direction y at several positions x/D. D is the gas chamber diameter and U_{avg} is the average inlet velocity of $6.8077\,\mathrm{ms}^{-1}$.

flow speed) in the recirculating gas. However, along the centre line, the temperatures are in very good agreement (Fig. 6). Because of the flow recirculation, the hot gases are now entrained towards the wall and have a large effect on the heat exchange with the solid. Fig. 8 shows the heat transfer along the inner wall surface, which is only due to the convective heat transfer. The heat transfer peaks near the reattachment point, where the flow practically impinges on the surface (see Fig. 9). Although the overall behaviour of the heat transfer is predicted similarly by both solvers, a notable difference of maximum 20% is noticed at the peak.

When radiation is activated both solvers predict higher wall heat transfer (Fig. 10) and lower flame temperature (Fig. 6). Both solvers show two peaks in radiative heat transfer of which the central peak is primarily due to the flame, while the downstream peak originates from the outlet boundary. Since the outlet has an emissivity value set at $0.5\,\mathrm{m}^{-1}$ (an estimate of the gas products) and its position right downstream of the flame (high temperature), it acts as an additional radiation source. Another agreement is that the convective heat transfer plays a minor role as the hot gas loses its energy through radiation before reaching the wall. The maximum heat transfer predictions differ by less than 10%. However, the discrepancies are more noticeable, especially when comparing the radiative heat transfer to the wall. There is a clear difference in both magnitude and location of the first peak. Also the local minimum and maxima are more pronounced in OpenFOAM. Comparing with the results of the case where radiation is switched off, it can be reasoned that the discrepancies in temperature, convective heat flux and total heat flux are affected by the different predictions of thermal radiation.

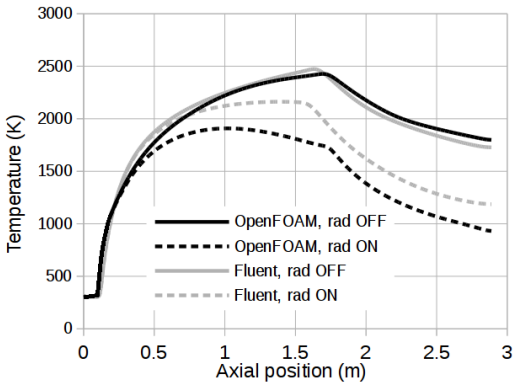

Figure 6: Temperature progression along the central axis of the gas chamber.

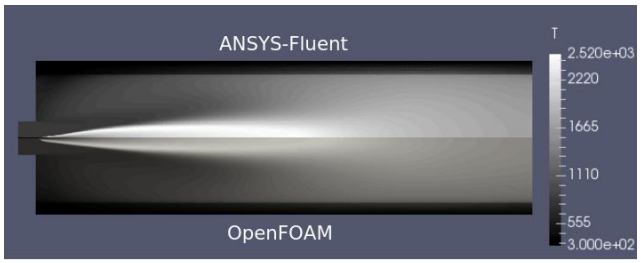

Figure 7: Comparison of the contour plots of the temperature (K) in Case 3 (radiation switched off).

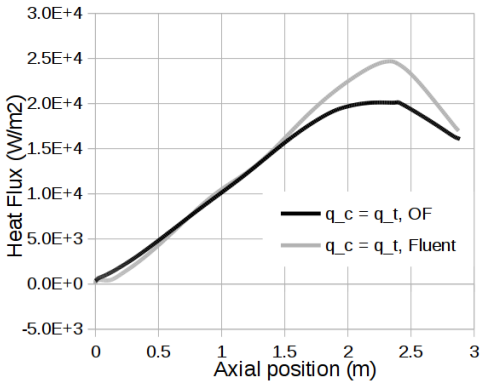

Figure 8: Heat flux (radiation OFF) along the inner wall surface of Case 3. q_c is the convective heat flux, which for this case is equal to the total heat flux q_t. OF = OpenFOAM.

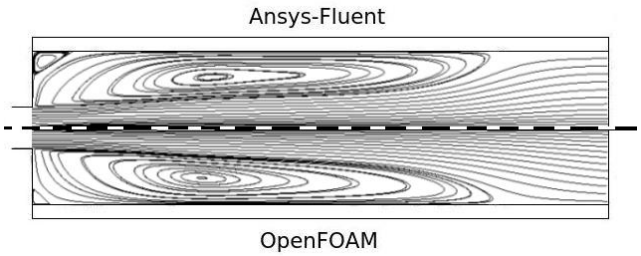

Figure 9: Comparison of the stream patterns

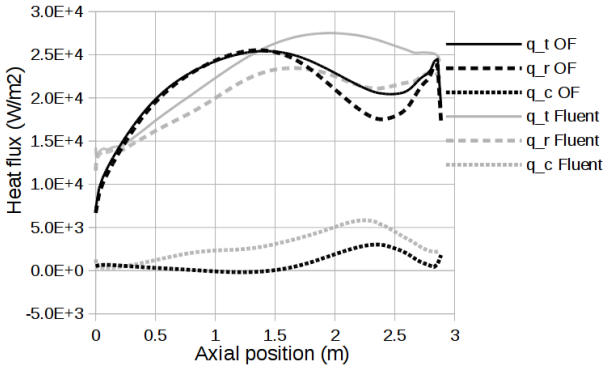

Figure 10: Heat flux (radiation ON) along the inner wall surface of Case 3. q_t, q_r and q_c are respectively the total, radiative and convective heat fluxes. OF = OpenFOAM.

Conclusions

This work has shown that OpenFOAM's standard solvers reactingFoam and chtMultiRegionFoam are succesfully implemented in the new solver multiRegionReactingFoam. This enables the modelling of combustion with conjugate heat transfer. The results of the new solver, with conjugate heat transfer turned off, are identical to reactingFoam and good agreement is shown with experiments when using the full GRI mechanism. With conjugate heat transfer switched on and without thermal radiation, good qualitative and quantitave agreements are shown with the results generated by Fluent. However, when thermal radiation is involved the agreements aggravate. Whether or not the wall function of the thermal diffusivity should be improved requires validation. In order to mitigate the influence of radiation by the outlet boundary it is recommended to add more distance between the outlet and the flame, or to use a colder reference temperature at the boundary. This can be enabled in OpenFOAM by modifying the code and creating an additional reference temperature field for the radiation model to extract from. Finally, since the temperature of the outer wall surface is fixed to a certain value, a realistic approach would be to change the temperature to a free variable and include radiative and convective heat losses at the boundary to allow a more accurate prediction of the heat distribution in the solid and the hot gas mixture.

Acknowledgements
The authors would like to thank Eric Daymo from Tonkomo LLC for developing the solver multiRegionReactingFoam and for his collaboration on debugging the solver in order to make it more robust.

Nomenclature

C	concentration	Y	mass fraction
c	constant	y	coordinate normal to the wall
c_p	specific heat capacity at constant pressure	δ	Dirac delta function
		ϵ	turbulence dissipation rate
E	Wall roughness parameter	Γ	diffusion coefficient
h	specific sensible enthalpy	γ	time ratio
I	radiation intensity	θ	constant
K	Von Kármán constant	κ	absorption coefficient
k	turbulent kinetic energy	λ	conductivity
p	pressure	μ	dynamic viscosity
Pr	Prandtl number	ν	kinematic viscosity
Q	heat flow rate	ξ	scattering coefficient
q	heat flux	ρ	density
R	(laminar) reaction rate	σ	Stefan-Boltzmann constant
r	radiant beam point	τ	shear stress tensor
S	modulus of the mean strain rate tensor	Φ	scattering phase function
s	radiant beam direction	ϕ	a scalar
T	temperature	χ	wavelength
t	time	Ω	solid angle
u	velocity		

Subcripts

b	black body	P	wall-adjacent fluid cell node coordinate
c	chemical reaction / convective	p	polynomial coefficient number
eff	effective	r	radiation
f	fluid	rad	radiation
i	1st Cartesian axis direction	s	solid
int	domain interface	t	turbulent
j	2nd Cartesian axis direction	w	wall
k	3rd Cartesian axis direction	α	chemical species
ℓ	reactant	β	chemical species
m	reaction product	τ	shear-
mix	turbulent mixing		

Superscripts

”	turbulent fluctuation component	$\sim$	Favre average
$\bar{}$	average	$+$	non-dimensional

References

[1] M. Pisaroni, R. Sadi, and D. Lahaye. Counteracting ring formation in rotary kilns. *Journal of Mathematics in Industry*, 2:3, 2012.

[2] H. Gao, A. Runstedtler, A. Majeski, R. Yandon, K. Zanganeh, and A. Shafeen. Reducing the recycle flue gas rate of an oxy-fuel utility power boiler. *Fuel*, 140:578–589, 2015.

[3] B. Danon, A. Swiderski, W. de Jong, W. Yang, and D.J.E.M. Roekaerts. Emission and efficiency comparison of different firing modes in a furnace with four HiTAC burners. *Combustion Science and Technology*, 183:686–703, 2011.

[4] D.A. Granados, F. Chejne, J.M. Mejía, C.A. Gómez, A. Berrío, and W.J. Jurado. Effect of flue gas recirculation during oxy-fuel combustion in a rotary cement kiln. *Energy*, 64:615–625, 2014.

[5] B. Krause, B. Liedmann, J. Wiese, S. Wirtz, and V. Scherer. Coupled three dimensional DEM–CFD simulation of a lime shaft kiln—calcination, particle movement and gas phase flow field. *Chemical Engineering Science*, 134:834–849, 2015.

[6] H.I. Kassem, K.M. Saqr, H.S. Aly, M.M. Sies, and M. Abdul Wahid. Implementation of the eddy dissipation model of turbulent non-premixed combustion in OpenFOAM. *International Communications in Heat and Mass Transfer*, 38:363–367, 2011.

[7] J.J. Keenan, D.V. Makarov, and V.V. Molkov. Modelling and simulation of high-pressure hydrogen jets using notional nozzle theory and open source code OpenFOAM. *International Journal of Hydrogen Energy*, 30:1–10, 2016.

[8] A.C. Benim, S. Iqbal, W. Meier, F. Joos, and A. Wiedermann. Numerical investigation of turbulent swirling flames with validation in a gas turbine model combustor. *Applied Thermal Engineering*, 110:202–2012, 2017.

[9] E. Fooladgar, C.K. Chan, and K.J. Nogenmyr. An accelerated computation of combustion with finite-rate chemistry using LES and an open source library for in-situ-adaptive tabulation. *Computers and Fluids*, 146:42–50, 2017.

[10] K.M. Pang, A. Ivarsson, S. Haider, and J. Schramm. Development and validation of a local time stepping-based PaSR solver for combustion and radiation modeling. In Proceedings of 8th International OpenFOAM Workshop, 2013.

[11] Z.H. Che Daud, D. Chrenko, F. Dos Santos, E.H. Aglzim, A. Keromnes, and L. Le Moyne. 3D electro-thermal modelling and experimental validation of lithium polymer-based batteries for automotive applications. *International Journal of Energy Research*, 40:1144–1154, 2016.

[12] G. Brösigke, A. Herter, M.Rädle, and J.U. Repke. Fundamental investigation of heat transfer mechanisms between a rolling sphere and a plate in OpenFOAM for laminar flow regime. *International Journal of Thermal Sciences*, 111:246–255, 2017.

[13] S.Sandler, B. Zajaczkowski, B.Bialko, and Z.M. Malecha. Evaluation of the impact of the thermal shunt effect on the U-pipe ground borehole heat exchanger performance. *Geothermics*, 65:244–254, 2017.

[14] C. Cintolesi, H. Nilsson, A. Petronio, and V. Armenio. Numerical simulation of conjugate heat transfer and surface radiative heat transfer using the P1 thermal radiation model: Parametric study in benchmark cases. *International Journal of Heat and Mass Transfer*, 107:956–971, 2017.

[15] Source code of chtMultiRegionReactingFoam. https://github.com/TonkomoLLC. accessed: 2017-01-15.

[16] E.A. Daymo and M. Hettel. Chemical reaction engineering with DUO and chtMultiRegionReactingFoam. 4th OpenFOAM User Conference 2016, Cologne-Germany, 2016.

[17] T. Poinsot and D. Veynante. *Theoretical and Numerical Combustion*. R.T. Edwards, 2nd edition, 2005.

[18] T.H. Shih, W.W. Liou, A. Shabbir, Z. Yang, , and J. Zhu. A new k-epsilon eddy-viscosity model for high reynolds number turbulent flows - model development and validation. *Computers Fluids*, 24(3):227–238, 1995.

[19] V. Golovitchev, N. Nordin, and F. Tao. Modeling of spray formation, ignition and combustion in internal combustion engines, annual report. Technical report, Chalmers University of Technology, Department of Thermo and Fluid Dynamics, 1998.

[20] M. Mancini, P.J. Coelho, and D.J.E.M. Roekaerts. Ercoftac best practice guide on cfd of combustion, chapter 4: Radiative heat transfer. Technical report, ERCOFTAC, 2015.

[21] H.K. Versteeg and W. Malalasekera. *An Introduction to Computational Fluid Dynamics:The Finite Volume Method*. Pearson Education Limited, 2nd edition, 2007.

[22] C.K. Westbrook and F.L. Dryer. Simplified reaction mechanisms for the oxidation of hydrocarbon fuels in flames. *Combustion Science and Technology*, 27:31–43, 1981.

[23] GRI-Mech 3.0. http://combustion.berkeley.edu/gri-mech/version30/text30.html.

[24] H. Schlichting. *Boundary-layer Theory*. McGraw-Hill, 7th edition, 1979.

[25] L. Davidson. *An Introduction to Turbulence Models*. Chalmers University of Technology, Department of Thermo and Fluid Dynamics, 2016.

[26] A.S. Dorfman. *Conjugate Problems in Convective Heat Transfer*. Taylor and Francis Group, LLC, 2010.

[27] Sandia flame D test description on the ERCOFTAC QNET-CFD wiki forums. http://qnet-ercoftac.cfms.org.uk/w/index.php/Description_AC2-09. accessed: 2016-07-01.

[28] B. Damstedt, J.M. Pederson, Hansen D, T. Knighton, J. Jones, C. Christensen, L. Baxter, and D.Tree. Biomass cofiring impacts on flame structure and emissions. *Proceedings of the Combustion Institute*, 31:2813–2820, 2007.